The Astrophysical Journal, 630:1133–1147, 2005 September 10

PREDICTED LIGHT CURVES FOR A MODEL OF SOLAR ERUPTIONS

Katharine K. Reeves and Terry G. Forbes
Institute for the Study of Earth, Oceans, and Space (EOS), University of New Hampshire, 39 College Road, Durham, NH 03824;
kreeves@unh.edu
Received 2005 March 8; accepted 2005 April 27

ABSTRACT

We determine the thermal radiation generated by a loss-of-equilibrium model for CMEs and eruptive solar flares. The magnetic configuration of the model consists of an outward-moving flux rope with a vertical current sheet below it. Reconnection at the sheet releases magnetic energy, some of which is converted into thermal energy that drives chromospheric evaporation along the newly connected field lines exiting the current sheet. The thermal energy release is calculated by assuming that all of the Poynting flux flowing into the reconnection region is eventually thermalized. We find that the fraction of the released magnetic energy that goes into thermal energy depends on the inflow Alfvén Mach number. The evolution of the temperatures and densities resulting from chromospheric evaporation is calculated using a simple evaporative cooling model. Using these temperatures and densities, we calculate simulated flare light curves for *TRACE*, the SXT on *Yohkoh*, and *GOES*. We find that when the background magnetic field strength is weak, the radiation emitted by the reconnected X-ray loops beneath a CME is faint. Additionally, it is possible to have two CMEs with nearly the same trajectories and speeds that have a significant difference in the peak intensities of their light curves. We also examine the relationship between the thermal energy release rate and the derivative of the soft X-ray light curve and discuss the implications for the Neupert effect.

Subject headings: Sun: coronal mass ejections (CMEs) — Sun: flares

1. INTRODUCTION

In order to investigate the radiative outputs in flares and coronal mass ejections (CMEs), we use a CME initiation model that is characterized by a loss of equilibrium in a configuration containing a flux rope (Forbes & Isenberg 1991; Forbes & Priest 1995). This loss of equilibrium is caused by a quasi-static evolution of the surface magnetic field driven by convective motions in the photosphere. After the eruption takes place, a current sheet forms and fields begin to reconnect. As was done previously (Lin & Forbes 2000), we assume that the reconnection rate is a prescribed function; however, any given reconnection model can easily be incorporated into this framework (Lin 2001).

There are several simplifying assumptions that are employed so that the equations governing the loss of equilibrium of the flux rope can be solved semianalytically. The model is two-dimensional, with simply connected background fields produced by oppositely oriented line currents in the chromosphere. This boundary condition allows for a substantial energy release ($\geq$8.6% of the free energy stored) even when reconnection is suppressed (Forbes et al. 1994). Also, we assume that the radius of the flux rope is small compared to the scale length of the system, and thus only first-order terms in the radius are used (Forbes & Priest 1995).

In this study gravity is neglected for simplicity, even though it can have a significant effect when the coronal field is weaker than 10 G or so (Reeves & Forbes 2005). The primary effects of gravity are to increase the amount of energy that can be stored and to decrease the speed of the CME (Lin 2004).

In the calculation of the dynamics of the eruption, we adhere to the assumption of previous models that the flux rope is treated as a projectile in order to determine its motion. Thus, the effects of MHD waves generated by this motion are not taken into account (Lin & Forbes 2000). In contrast to previous work on this model, we consider the effect of reconnection heating on the eruption dynamics. We calculate this heating by assuming that there is complete thermalization of the Poynting flux in the current sheet; thus, the acceleration of the flux rope by outflow from the reconnection region is ignored. The effect of outflow jets on the flux rope motion could be treated by incorporating reverse current sections at the tips of the current sheet (Priest & Forbes 1992), but this would significantly add to the complexity of our calculations with only a relatively small gain in accuracy.

Using the calculated thermal energy produced by reconnection, we model the evaporation and cooling of the plasma in the reconnected loops below the CME and ultimately obtain simulated light curves. We use a model for the evaporation and cooling dynamics developed by Cargill et al. (1995), which is powerful because of its simplicity, especially when calculating the cooling profiles of large numbers of loops (Reeves & Warren 2002). It is limited, however, in that the conductive and radiative cooling phases are assumed to be separate, and an empirical law is used to relate the temperature and density in the radiative cooling phase.

Other calculations of thermal energy and chromospheric evaporation in flares have been performed. Yokoyama & Shibata (2001) used a two-dimensional MHD simulation to determine the thermal energy release due to magnetic reconnection and chromospheric evaporation and conclude that the thermal energy release rate is approximately linear in time. In contrast to the models we base our work on, their simulation starts with the magnetic field already in an open state, and they do not include a loss of equilibrium initiation method. Hori et al. (1997, 1998) used several one-dimensional hydrodynamic loop simulations to create a "pseudo–two-dimensional" flare arcade and found that this multiloop approach was better than a single loop at recreating the observed soft X-ray emission (Hori et al. 1997) and Ca XIX resonance line emission (Hori et al. 1998). The heating rate for the loops in this "pseudo–two-dimensional" calculation was arbitrarily assumed to be a Gaussian in space and a step function in time.

The outline of the paper is as follows. In § 2.1 we give the mathematical form for the magnetic field configuration. In § 2.2

we describe the energetics of the model, and in § 2.3 we describe the calculation of the trajectories of the flux rope and the tips of the current sheet. The Cargill cooling model is described in § 2.4, and calculation of the initial conditions of the plasma in the reconnected loops is detailed in § 2.5. The results and discussion are given in § 3, and the conclusions are presented in § 4.

2. CALCULATIONS

2.1. *Magnetic Field Model*

Prior to the eruption of the CME, the system consists of two line sources embedded in the chromosphere and a flux rope containing a current I located at a distance h above the chromosphere. The line sources are brought together quasi-statically, allowing the system to evolve through a series of equilibria, until a loss of equilibrium takes place, initiating the CME. After the eruption, the field has the form previously employed by Lin & Forbes (2000), shown in Figure 1. The line currents remain fixed at a distance 2λ apart. This distance is the separation at which the loss of equilibrium occurs, and it is given by $\lambda = 0.9695\lambda_0$, where $2\lambda_0$ is the separation of the line sources at the point of maximum current in the flux rope, a convenient normalization point (Forbes & Priest 1995). A vertical current sheet connects the flare loops at the bottom of the configuration with the field lines surrounding the flux rope at the top. The bottom tip of the current sheet is at a height p and the upper tip is at a height q. This magnetic field is prescribed in complex notation by

$$B_y + iB_x = \frac{2iA_0\lambda(h^2+\lambda^2)\sqrt{(\zeta^2+p^2)(\zeta^2+q^2)}}{\pi(\zeta^2-\lambda^2)(\zeta^2+h^2)\sqrt{(\lambda^2+p^2)(\lambda^2+q^2)}}, \quad (1)$$

where $\zeta = x + iy$ and A_0 is the source field strength. This form of the magnetic field gives rise to an expression for the vector potential (see Lin 2001, Appendix A):

$$\begin{aligned} A(\zeta) &= -\int B(\zeta)d\zeta \\ &= \frac{4iA_0\lambda}{\pi(q-p)}\sqrt{\frac{(\lambda^2+p^2)}{(\lambda^2+q^2)}}\left\{F\left(\sin^{-1}\left(\sqrt{\frac{f_p(\zeta)}{PQ}}\right),\ PQ\right)\right. \\ &\quad + \frac{\lambda}{q}(p-q)(\lambda^2+h^2)F\left(i\sinh^{-1}\left(\frac{\zeta}{p}\right),\ \frac{p}{q}\right) \\ &\quad + \frac{\lambda}{h^2 q}(q-p)H_{PQ}^2\Pi\left(i\sinh^{-1}\left(\frac{\zeta}{p}\right),\ \frac{p^2}{h^2},\ \frac{p}{q}\right) \\ &\quad - 2p(\lambda^2+p^2)\left[\Pi\left(\sin^{-1}\left(\sqrt{\frac{f_p(\zeta)}{PQ}}\right),\ f_p(\lambda)PQ,\ PQ\right)\right. \\ &\quad \left.\left. + \Pi\left(\sin^{-1}\left(\sqrt{\frac{f_p(\zeta)}{PQ}}\right),\ \frac{PQ}{f_p(\lambda)},\ PQ\right)\right]\right\}, \end{aligned} \quad (2)$$

where F and Π are incomplete elliptic integrals of the first and third kinds, respectively, $H_{PQ} = [(h^2-p^2)(h^2-q^2)]^{1/2}$, $PQ = (p+q)/(p-q)$, and $f_p(z) = (p-iz)/(p+iz)$. This expression for A is a more compact form of the expression given in Lin & Forbes (2000). The current in the flux rope is (Lin & Forbes 2000)

$$I = \frac{c\lambda A_0}{2\pi h}\frac{\sqrt{(h^2-p^2)(h^2-q^2)}}{\sqrt{(\lambda^2+p^2)(\lambda^2+q^2)}}. \quad (3)$$

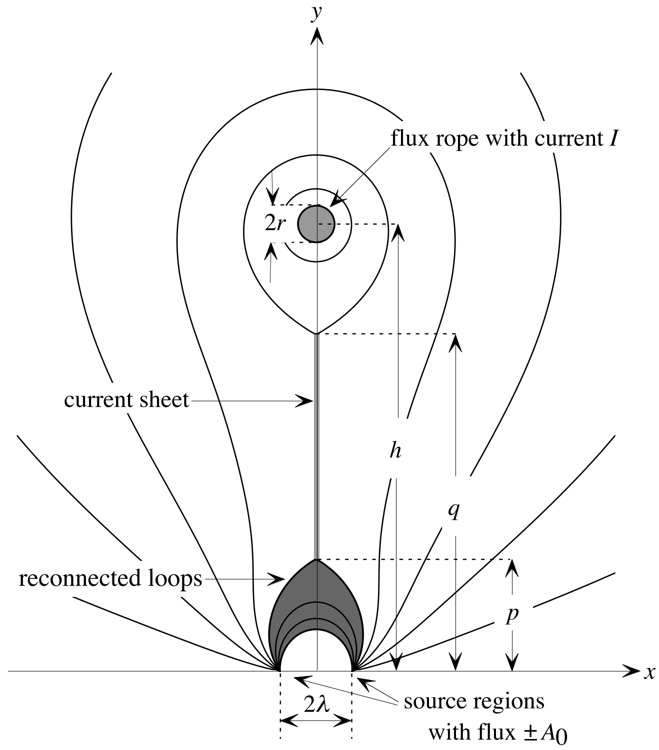

FIG. 1.—Magnetic configuration for the model, after Lin & Forbes (2000).

The above field has the property that $A(x, 0)$ remains invariant as h, p, and q are varied, so that the field is line-tied at the base.

2.2. *Energetics*

At any given time the total energy of the system is given by

$$W_{\rm mag} + W_{\rm KE} + W_{\rm th} = W_0, \quad (4)$$

where $W_{\rm mag}$ is the free magnetic energy, $W_{\rm th}$ is the thermal energy, $W_{\rm KE}$ is the kinetic energy of the flux rope, and W_0 is the initial energy in the system. Thus,

$$\frac{d}{dt}(W_B + W_{\rm KE} + W_{\rm th}) = 0. \quad (5)$$

The rate of change of the kinetic energy of the flux rope is related to its altitude, h, by

$$\frac{dW_{\rm KE}}{dt} = \frac{d}{dt}\left(\frac{1}{2}m\dot{h}^2\right) = m\ddot{h}\dot{h} = F\dot{h}, \quad (6)$$

where m is the mass of the flux rope and F is given by

$$\begin{aligned} F &= \frac{I}{c}B_{\rm ext} \\ &= \frac{A_0^2\lambda^2}{2h\pi^2(\lambda^2+p^2)(\lambda^2+q^2)}\left\{\frac{(h^2-p^2)(h^2-q^2)}{2h^2}\right. \\ &\quad \left. - \frac{[(\lambda^2+p^2)(h^2-q^2)+(\lambda^2+q^2)(h^2-p^2)]}{\lambda^2+h^2}\right\}. \end{aligned} \quad (7)$$

Here $B_{\rm ext}$ is the external field due to the field outside the flux rope, which includes not only the sources at $\pm\lambda$ but also a surface current at $y = 0$ (see Lin & Forbes 2000; Forbes & Isenberg

1991; Isenberg et al. 1993; Lin et al. 1998). Note that the field due to the surface current is equivalent to the field of an image current at a depth h below the chromosphere.

To calculate the other two terms in equation (5), we use

$$\frac{d}{dt} = \frac{\partial}{\partial h}\dot{h} + \frac{\partial}{\partial p}\dot{p}, \tag{8}$$

where the first term represents changes due to the motion of the flux rope, while the second represents those due to the reconnection of the current sheet. For the thermal energy,

$$\frac{\partial W_{\rm th}}{\partial h}\dot{h} = 0, \tag{9}$$

since if p is constant, there is no reconnection and, therefore, no heating. Thus,

$$\frac{dW_{\rm th}}{dt} = \frac{\partial W_{\rm th}}{\partial p}\dot{p}. \tag{10}$$

Now, if we rewrite equation (5) holding h constant, we get

$$\left.\frac{\partial W_{\rm mag}}{\partial t}\right|_h + \frac{\partial W_{\rm th}}{\partial p}\dot{p} = 0. \tag{11}$$

Using equations (10) and (11) and the fact that

$$\left.\frac{\partial W_{\rm mag}}{\partial t}\right|_h = -S(t), \tag{12}$$

where $S(t)$ is the integral of the Poynting flux along the current sheet, the rate of change of the thermal energy is given by

$$\frac{dW_{\rm th}}{dt} = S(t). \tag{13}$$

Combining equations (5), (6), (7), and (13), we write

$$\begin{aligned}\frac{dW_{\rm mag}}{dt} = \frac{-A_0^2\lambda^2}{2h\pi^2(\lambda^2+p^2)(\lambda^2+q^2)}&\left\{\frac{(h^2-p^2)(h^2-q^2)}{2h^2}\right.\\ &\left.-\frac{[(\lambda^2+p^2)(h^2-q^2)+(\lambda^2+q^2)(h^2-p^2)]}{\lambda^2+h^2}\right\}\dot{h}\\ &-S(t).\end{aligned} \tag{14}$$

This equation is just a statement of Poynting's theorem for this particular system.

In order to solve the differential equations for $W_{\rm mag}$ and $W_{\rm th}$, we need to know their initial values. If we take t_n to be the time when the neutral point forms, $W_{\rm th}(t_n) = 0$ since there is no current sheet at this time. The magnetic energy at time t_n is given by

$$W(h_n, J_n) = \left(\frac{A_0}{\pi}\right)^2\left[J_n^2 \ln\left(\frac{2h_nJ_n}{r_0}\right) + \frac{1}{2}J_n^2 + \frac{1}{4}\right], \tag{15}$$

where J_n and h_n are the flux rope current and height at t_n, normalized to their values at the maximum current point. The parameter r_0 is the radius of the flux rope at the maximum current point. This equation is found by integrating the forces on the flux rope and making use of the approximation that the flux rope radius is given by r_0/J (for a detailed derivation see Forbes & Priest 1995).

To calculate the power dissipated in the flare loops, we need to calculate the Poynting flux in the current sheet, namely,

$$S(t) = \frac{c}{2\pi}E_z(t)\int_{p(t)}^{q(t)} B_y(0,\ y,\ t)\,dy, \tag{16}$$

where the magnetic field along the sheet is given by equation (1) with $x = 0$. The electric field $E_z(t)$ can be taken outside the integral because it is uniform along the sheet. From Faraday's law $E_z(t) = -(1/c)\partial A_{\rm cs}/\partial t$, where $A_{\rm cs}$ is the magnitude of the vector potential at the sheet at any given time.

To complete the model, we need to prescribe the rate of reconnection at the current sheet. Here we assume that it is given by

$$E_z = M_{\rm A}V_{\rm A}(0,\ y_0)B_y(0,\ y_0)/c, \tag{17}$$

where $M_{\rm A}$, the Mach number, is assumed to be a constant, $y_0 = (p+q)/2$ is the midpoint of the current sheet, and $V_{\rm A}$ is the Alfvén speed at the midpoint. This assumed form for the reconnection rate is not the only choice, however. Other assumptions based on Sweet-Parker or Petschek theory are possible (Lin 2001), but we use the form of equation (17) here in order to facilitate comparison with the previous published findings.

Inserting equations (1) and (17) into equation (16) and calculating the integral, we obtain

$$\begin{aligned}S(t) = \frac{-8iM_{\rm A}A_0^3\lambda^3}{2\pi^4\sqrt{4\pi\rho(y_0)}}&\frac{(h^2+\lambda^2)^3(p^2-y_0^2)(q^2-y_0^2)}{L_{PQ}^3(y_0^2+\lambda^2)^2(y_0^2-h^2)^2}\\ \times&\left\{\frac{-F(\sin^{-1}(p/q),\ q/p)+K(q/p)}{p}\right.\\ &+\frac{2i(h^2-q^2)K((p-q)/(p+q))}{(h^2+\lambda^2)(p+q)}\\ &-\frac{L_{PQ}^2[\Pi(-q^2/\lambda^2,\ q/p)-\Pi(q^2/\lambda^2,\ -\sin^{-1}(p/q),\ q/p)]}{\lambda^2(h^2+\lambda^2)p}\\ &+\frac{2ip(h^2-q^2)}{h(h^2+\lambda^2)(p+q)}\left[\Pi\left(\frac{(h+p)(q-p)}{(h-p)(q+p)},\ \frac{(p-q)}{(p+q)}\right)\right.\\ &\left.\left.-\Pi\left(\frac{(h-p)(q-p)}{(h+p)(q+p)},\ \frac{(p-q)}{(p+q)}\right)\right]\right\},\end{aligned} \tag{18}$$

where K and F are complete and incomplete elliptic integrals of the first kind, respectively, Π is either a complete or incomplete elliptic integral of the third kind (depending on the number of arguments), $L_{PQ} = [(\lambda^2+p^2)(\lambda^2+q^2)]^{1/2}$, and p, q, and h are functions of time.

2.3. *Trajectories*

Although previous versions of this model did not consider the thermal energy generated by reconnection and evaporation, the equations governing the evolution of p, q, and h as functions of time remain unchanged when heating is included because only the work done by the magnetic force on the flux rope affects the trajectories. However, the total magnetic energy release is now different than before because there is an additional component, corresponding to the Poynting flux into the current sheet, that must now be included. This component exists even if the flux rope does not move since it arises only from the energy released by the diminution of the current sheet as reconnection proceeds.

The equation for q is derived from the condition that the tips of the current sheet are null points, while the equation for p comes from Faraday's law and the function that prescribes the reconnection rate. The conservation of flux between the bottom of the flux rope and the surface during the evolution of the system determines I (and thus q since the two are related through eq. [3]).

Faraday's law can be written as

$$E_z = -\frac{1}{c}\frac{\partial A_{\rm cs}}{\partial t} = -\frac{1}{c}\frac{\partial A_{\rm cs}}{\partial h}\dot{h}, \tag{19}$$

where $A_{\rm cs} = A(0,\ p \le y \le q)$ is the magnitude of the vector potential along the current sheet and $\dot{h} = dh/dt$. In terms of partial derivatives of $A_{\rm cs}$ we obtain

$$E_z = -\frac{\dot{h}}{c}\left(\frac{\partial A_{\rm cs}}{\partial p}p' + \frac{\partial A_{\rm cs}}{\partial q}q' + \frac{\partial A_{\rm cs}}{\partial h}\right), \tag{20}$$

where $p' = dp/dh$ and $q' = dq/dh$.

Conservation of flux is implemented by requiring that the flux remain constant at the bottom of the flux rope:

$$A_R = A(0,\ h - r) = \text{const}, \tag{21}$$

where r is the radius of the flux rope at all times. Taking the total derivative with respect to time on both sides of the above equation gives

$$\frac{\partial A_R}{\partial p}p' + \frac{\partial A_R}{\partial q}q' + \frac{\partial A_R}{\partial h} = 0. \tag{22}$$

Combining equations (20) and (22), we find expressions for p' and q':

$$p' = \frac{\left(cE_z/\dot{h} + \partial A_{\rm cs}/\partial h\right)\partial A_R/\partial q - (\partial A_R/\partial h)(\partial A_{\rm cs}/\partial q)}{(\partial A_R/\partial p)(\partial A_{\rm cs}/\partial q) - (\partial A_R/\partial q)(\partial A_{\rm cs}/\partial p)}, \tag{23}$$

$$q' = \frac{(\partial A_R/\partial h)(\partial A_{\rm cs}/\partial p) - \left(cE_z/\dot{h} + \partial A_{\rm cs}/\partial h\right)\partial A_R/\partial p}{(\partial A_R/\partial p)(\partial A_{\rm cs}/\partial q) - (\partial A_R/\partial q)(\partial A_{\rm cs}/\partial p)}, \tag{24}$$

where the electric field E_z is given by equation (17).

To determine the speed of the flux rope, we use Newton's second law applied to the mass, m, of the flux rope:

$$F = m\frac{d^2h}{dt^2}, \tag{25}$$

where F is given by equation (7). Since d^2h/dt^2 can be written as $\dot{h}\dot{h}'$, with $\dot{h}' = d\dot{h}/dh$, we set $\dot{h}' = F/m\dot{h}$. We combine this expression with equations (23) and (24) to get expressions that are functions of time:

$$\begin{aligned} \frac{dp}{dt} &= p'\dot{h}, \\ \frac{dq}{dt} &= q'\dot{h}, \\ \frac{d\dot{h}}{dt} &= \dot{h}'\dot{h}, \\ \frac{dh}{dt} &= \dot{h}. \end{aligned} \tag{26}$$

Thus, the original set of equations governing the dynamics of the system, consisting of equations (1), (3), (7), (19), and (21), are reduced to a set of equations describing the motion of the flux rope and the dynamics of the current sheet.

The set of four differential equations given by equation (26), along with equations (13) and (14), are solved numerically (using the Mathematica routine NDsolve) to find the trajectories of the flux rope and the two ends of the current sheet (h, p, and q), the velocity of the flux rope ($\dot{h}$), the magnetic energy stored in the configuration ($W_{\rm mag}$), and the thermal energy dissipated in the current sheet ($W_{\rm th}$).

2.4. *Loop Cooling Model*

To model the cooling of the plasma in the loops, we use a simple model based on that of Cargill et al. (1995), which has been used previously to calculate the cooling in a multiloop postflare arcade (Reeves & Warren 2002). This model assumes that the cooling of the plasma is separated into a conductive cooling phase followed by a radiative cooling phase. Cooling times are calculated for each of these phases, and the process with the shortest cooling time dominates at that point in the cooling.

The conductive cooling phase includes the effect of chromospheric evaporation whereby the flare heats chromospheric material and causes it to expand rapidly up into the corona (see, for example, Antiochos & Sturrock 1978). The Cargill et al. (1995) model assumes that the pressure is constant in the loops as a function of time and that the temperature is given by

$$T(t + dt) = T(t)\left(1 + \frac{dt}{\tau_c}\right)^{-2/7}, \tag{27}$$

where dt is the length of the time step, τ_c is the conductive cooling time (given by $4\times10^{10} nL/T^{5/2}$), n is the electron density in the loop, and L is the loop half-length. Since the pressure is assumed constant in the loops, the density at the end of each time step is given by

$$n(t + dt) = n(t)\left[\frac{T(t)}{T(t + dt)}\right]. \tag{28}$$

During the radiative cooling phase we assume that the temperature in the loop is proportional to the square of the density. This assumption is the same as in Cargill et al. (1995) and Reeves & Warren (2002), and it is an empirical relation derived from hydrodynamic simulations. Thus, the density at the end of each time step is given by

$$n(t + dt) = n(t)\left[\frac{T(t + dt)}{T(t)}\right]^{1/2} \tag{29}$$

and the corresponding temperature by

$$T(t + dt) = T(t)(1 + \eta\, dt)^{2/[2(2-\alpha)-3]}, \tag{30}$$

where α is a function of T and is related to the radiative loss function by $P_{\rm rad} = \chi T^{\alpha}$. [The form of $\alpha(T)$ we use here is a custom function, a full description of which can be found in Reeves & Warren 2002.] Here η is a function of α and is inversely proportional to the radiative cooling time, $\tau_r = 3k_{\rm B}T^{1-\alpha}/n\chi$. More information on these functions and their derivations can be found in the Appendix of Cargill et al. (1995).

2.5. *Calculation of Initial Plasma Conditions in the Loops*

As described above, the cooling model requires an initial temperature and density to be specified for each loop. The initial density in the loop depends on the form chosen for the coronal atmosphere. The Lin & Forbes (2000) model used an atmosphere that falls off exponentially with height, but recently Lin (2002) modified those calculations to incorporate the more realistic atmosphere of Sittler & Guhathakurta (1999), which is based on observations from *Skylab* and *Ulysses*. In this atmosphere the density in the corona falls off exponentially near the surface of the Sun and as $1/r^2$ at large distances from the Sun. This density model provides separate descriptions for polar coronal holes and closed field regions at the equator. Here we use the coronal hole model as it best approximates the open field conditions (i.e., the transient coronal holes) created at the onset of a CME. For each loop an initial density is determined by finding the height of the loop apex and calculating the coronal density at that height according to the atmospheric model described above.

In order to determine the initial temperature in each loop, we first calculate the initial loop pressure by relating the Poynting flux into the current sheet to the thermal energy input rate:

$$\frac{3}{2}\int_{\text{loop}} P|v_n|\,dl = \frac{cE_0}{2\pi}\int_p^q B_y\,dy = S(t), \tag{31}$$

where P is the gas pressure along the loop and v_n is the normal component of the apparent flow through the separatrix field line (the line that maps to the Y-point at the lower tip of the current sheet). The integral on the left-hand side is a path integral along the length of the loop from the base to the top.

The apparent velocity of the flow normal to the reconnected field line, v_n, is the difference between the convective velocity of the plasma, v_{conv}, and the velocity of the separatrix, v_{sep}, in the rest frame of the Sun. In two dimensions the magnitudes of these velocities can be expressed as

$$v_{\text{conv}} = \left(-\frac{\partial A}{\partial t}\frac{1}{|\nabla A|}\right)_{A=A_0},$$
$$v_{\text{sep}} = \left[\left(-\frac{\partial A}{\partial t} + cE_0\right)\frac{1}{|\nabla A|}\right]_{A=A_0}. \tag{32}$$

The first equation comes from the fact that $dA/dt = \partial A/\partial t + \boldsymbol{v}_{\text{conv}} \cdot \nabla A = 0$ along a field line frozen to the plasma, while the second equation comes from the fact that $dA_0/dt = \partial A_0/\partial t + \boldsymbol{v}_{\text{sep}} \cdot \nabla A_0 = cE_0$ at the separatrix. Thus, v_n is given by

$$|v_n| = |v_{\text{conv}} - v_{\text{sep}}| = c\frac{|E_0|}{|B|}, \tag{33}$$

since $|\nabla A| = B$ in two dimensions. If we assume that the pressure is uniform along the loop, P can be taken out of the integral in equation (31). Solving for P then gives

$$P = \frac{\int_p^q B_y\,dy}{3\pi\int_{\text{loop}} dl/B}. \tag{34}$$

The initial density determined from the coronal atmospheric model, together with the pressure in the loop and the ideal gas law, gives the initial temperature in the loop. Using these inputs along with the Cargill cooling model, we calculate the evolution of the temperatures and densities as a function of time for each loop in the reconnected arcade.

3. RESULTS AND DISCUSSION

We choose the physical parameters of our simulations to be commensurate with the observed properties of CMEs. For most of the results described in this paper the following quantities were used:

$$M_{\text{A}} = 0.025, \quad \lambda_0 = 2\times10^9 \text{ cm},$$
$$m = 2.1\times10^{16} \text{ g}, \quad \rho = 1.67\times10^{-16} \text{ g cm}^{-3},$$
$$L = 10^{10} \text{ cm},$$

where M_{A} is the Alfvén Mach number at the midpoint of the current sheet, ρ is the proton density at the base of the corona, λ_0 is the half-distance between the line sources at the maximum current point, and m and L are the mass and length of the flux rope. The length and mass of the flux rope are the same as in Lin & Forbes (2000). We choose a value of ρ that is 100 times smaller than that of Lin & Forbes (2000) because this value is more consistent with the observed coronal density of the open field structures created by the CME. Since decreasing the density increases the ambient Alfvén speed, we have also adjusted the value of M_{A} to match the values inferred from observation (e.g., Dere 1996; Yokoyama et al. 2001).

We use several average background magnetic field strengths in order to investigate the effects of the background field on the flux rope trajectories, energy release, and resulting light curves. The background magnetic field is related to the flux in the photospheric source regions and is given by $B = A_0/(\pi\lambda_0)$. We choose values that range from 12 to 120 G.

The trajectories and flux rope velocities for the calculations with background fields of 12 and 120 G are shown in Figure 2. They are very similar in character to those found in Lin (2002), even though we are using somewhat different physical parameters. Lin (2002) and others (see, e.g., Forbes 2003) have assumed that the inclusion of heating in this model would diminish the flux rope kinetic energy and hence change the velocity and trajectories. Although the production of thermal energy depletes the stored magnetic energy, it does not affect the work done accelerating the flux rope. Thus, the trajectories of the flux rope and the current sheet are unaffected by the inclusion of the thermal energy term in the system of equations.

As shown in Lin (2002) and Figure 2, a decrease in the background field strength in this model causes the speed that the CME reaches to decrease if all other parameters are kept the same. Consequently, for the parameters we are using, the cases with high background fields correspond to fast CMEs and lower fields correspond to slow CMEs. We have examined several cases of varying background field strength in order to give a range of CME speeds, including the 12 and 120 G background field cases shown in Figure 2, which have CME speeds of 300 and 3000 km s^{-1}, respectively. Also considered, but not pictured in Figure 2, are cases with 50 and 85 G background fields that have CME speeds of about 1200 and 2100 km s^{-1}, respectively. Thus, we can relate our model results to observations that span the range of observed CME speeds.

3.1. *Energetics*

The energy budget for this CME model is calculated and shown in Figure 3 for the 12 and 120 G background cases. There is more total energy in the system with the 120 G background field, and a greater percentage of the total energy is released and

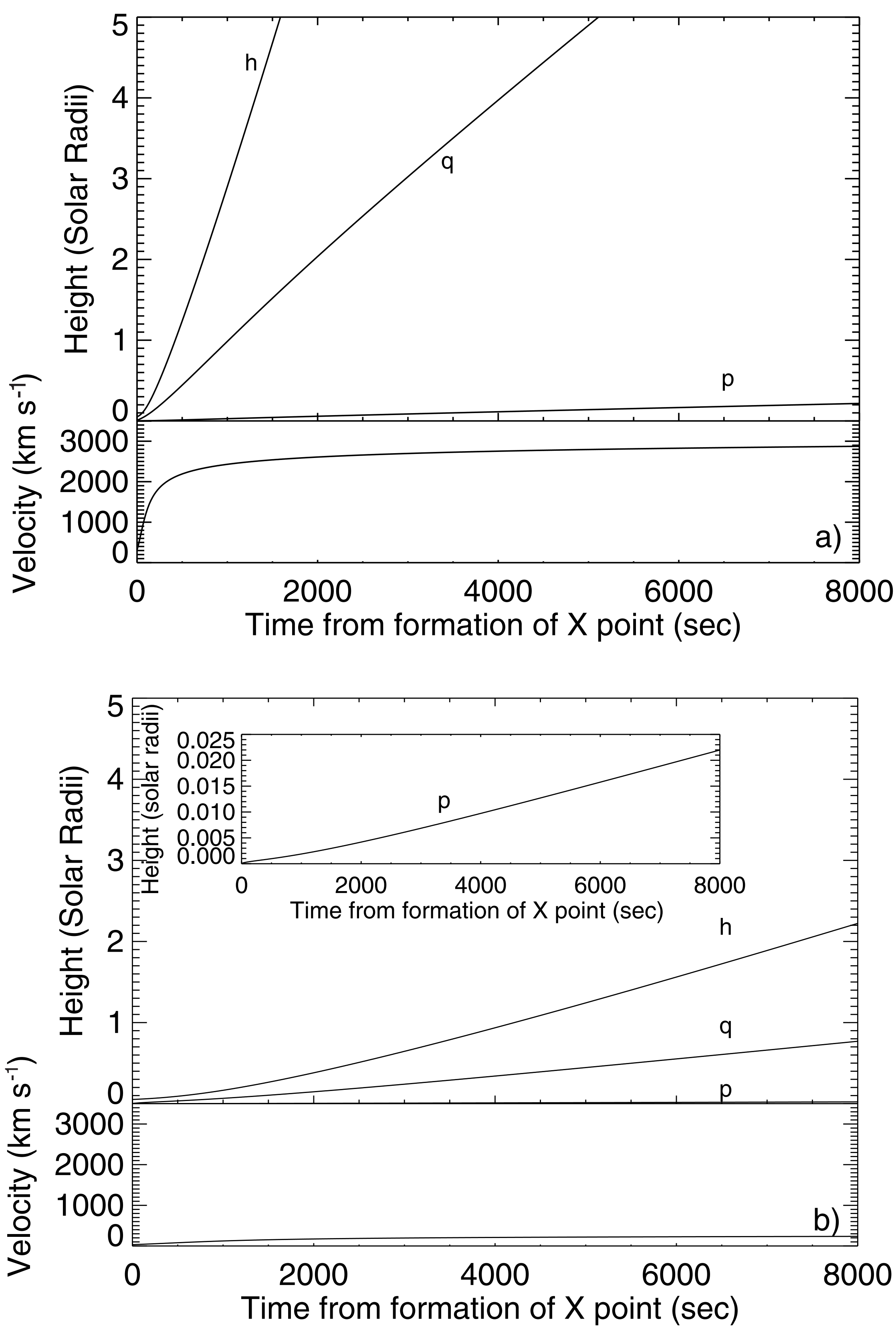

FIG. 2.—Plots of the height of the flux rope, h, the top and bottom tips of the current sheet (q, p), and the velocity of the flux rope as a function of time. Panels (a) and (b) show the trajectories for the strongest (120 G) and weakest (12 G) background fields, respectively. The inset in panel (b) is the height of the bottom tip of the current sheet shown on an expanded scale. In all cases $M_A = 0.025$.

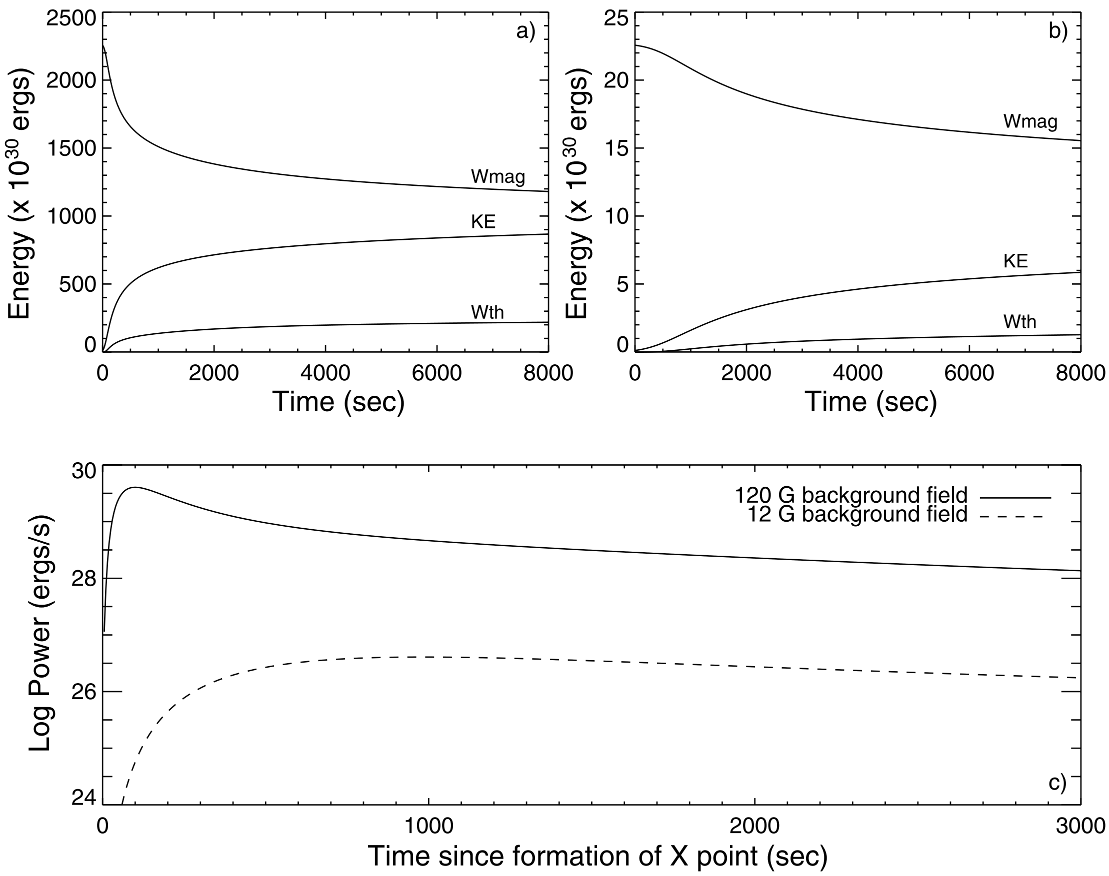

FIG. 3.—Panels (*a*) and (*b*) show the magnetic and kinetic energy of the flux rope and thermal energy as a function of time for the strongest (120 G) and weakest (12 G) background fields studied, respectively. Panel (*c*) shows the power output from the thermal energy as a function of time for the 120 G case (*solid line*) and the 12 G case (*dashed line*). In all cases $M_A = 0.025$.

turned into kinetic and thermal energy than in the 12 G case. All of the energy stored in the system is not released in the eruption, however, so we must be careful to distinguish between the total energy stored in the system and the energy that is released and available for conversion into heat or work. In the cases where the flux rope achieves escape velocity (as it does for the parameters and background field strengths mentioned above), the energy released (W_{mag} in Fig. 3) approaches an asymptotic value at long times. In all four cases that were examined, the thermal energy was 17%–20% of the released energy near this asymptotic limit. This percentage depends on the reconnection rate, as well as the mass of the flux rope.

The power associated with the thermal energy release is shown in Figure 3*c*. The rate at which thermal energy is released is faster for the case with the higher background field strength, and the shape of the curve for this case is very reminiscent of stellar and solar flare light curves. The weak background field case has a much slower energy release rate, and the peak power is several orders of magnitude smaller, indicating that flares associated with CMEs from weak magnetic field regions may be quite faint. These results are not the same as those of Yokoyama & Shibata (2001), who found that the energy release rate is a linear function of time; however, they only model the reconnection process and do not include the flux rope dynamics. Lin (2002) reached conclusions similar to ours regarding the power released in the flare, but it should be noted that the power referred to in that paper was the power associated with the work done on accelerating the flux rope and did not include the thermal energy release.

The fraction of released energy that is converted into thermal energy is affected by the value of M_A used in this model, as shown for three different cases in Figure 4. We plot the kinetic energy and thermal energy for M_A values of 0.1, 0.006, and 0.001, with a background field of 120 G and all of the other input parameters the same as described at the beginning of § 3. As M_A is decreased, the percentage of released energy that is converted to thermal energy increases. In the bottom panel of Figure 4, the reconnection rate is relatively fast ($M_A = 0.1$), and most of the energy is converted into the motion of the flux rope, with only a small fraction of the released energy converted into heat. In the middle panel, where $M_A = 0.006$, the distribution of energy into kinetic and thermal energy is almost evenly split. When the reconnection rate is very slow, as in the top panel of Figure 4 with $M_A = 0.001$, the bulk of the released energy goes into heating the flare plasma. When the reconnection rate is this slow, the flux rope decelerates because of the magnetic tension that builds up as the current sheet forms. This process causes the kinetic energy to be converted back into magnetic energy that is associated with the stretching of the sheet.

The results presented in Figure 4 are useful in illustrating the effects of varying the parameter M_A in our model. In the limit that $M_A \to \infty$, reconnection is uninhibited, allowing magnetic field lines to reconnect at the X-point without forming a current sheet. Therefore, in this limit, no plasma heating occurs.

The behavior of the system in the opposite limit, when $M_A \to 0$, is harder to ascertain using this model. When M_A becomes too low in our calculations, the flux rope can decelerate or even oscillate a few times before escaping (Lin & Forbes 2000; Lin 2002). This deceleration occurs in the case shown in the top panel of Figure 4 and is the reason for the initial peak and decrease in the kinetic energy. When $M_A = 0$, there is no reconnection and the

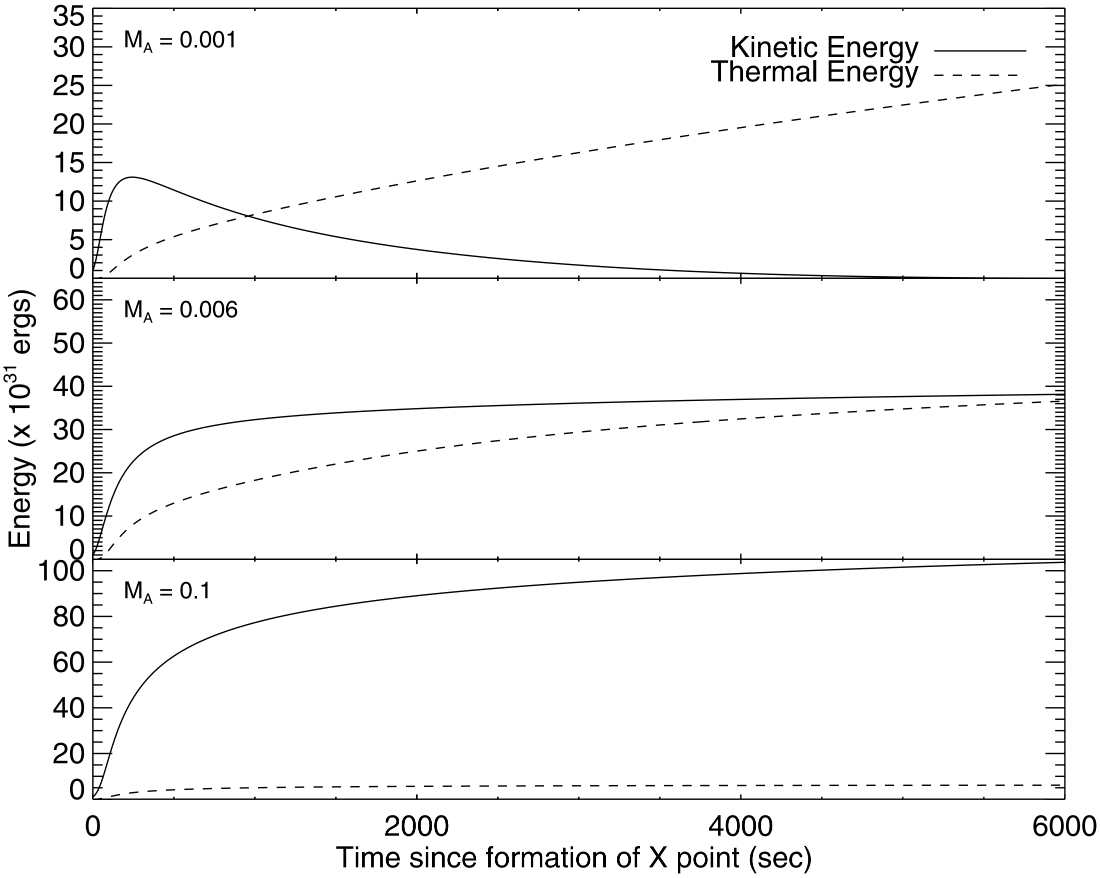

FIG. 4.—Kinetic energy (*solid line*) and thermal energy (*dashed line*) as a function of time for M_A values of 0.001 (*top*), 0.006 (*middle*), and 0.1 (*bottom*). For all cases there is a 120 G background field.

flux rope continually oscillates (Forbes & Priest 1995; Lin & Forbes 2000). This oscillatory behavior is due to the two-dimensional nature of the model, and it makes it difficult to evaluate the fraction of the thermal energy that is released when the Mach number is low. However, we do know that no thermal energy is released when $M_A = 0$ because the Poynting flux into the current sheet is zero in that case. In a more realistic three-dimensional model oscillations would not necessarily occur. The flux rope in our two-dimensional model cannot escape unless reconnection occurs, but in three dimensions the overlying field can slip to the side (out of the plane in our figures) so that the tension acting on the flux rope is greatly reduced (Sturrock et al. 2001). Thus, in a three-dimensional model there may be some value for M_A where the fractional thermal energy release is maximized.

The strength of the background magnetic field does not affect the fraction of energy that is released as thermal energy. The plot in Figure 4 shows the thermal and kinetic energies for cases with a background field of 120 G; however, when other background magnetic field strengths are used with the same values for M_A, very similar fractional thermal energies are obtained. Thus, the reconnection rate is more important than the background magnetic field strength in determining the fraction of released energy that is transformed into thermal energy, although of course the magnitude of the thermal energy is determined in part by the background magnetic field strength, as is clearly shown in Figure 3.

3.2. *Light Curves*

The calculated thermal energy release rate is used to determine initial temperatures and densities in the lower set of loops in Figure 1 for the four different background magnetic field strengths. The evolution of the temperatures and densities in these loops due to chromospheric evaporation and conductive and radiative cooling of the plasma is then calculated using the Cargill model, as described in the previous section. The arcade of loops is made up of approximately 2000 loops, with a 5 s spacing in time between each loop. Some snapshots of the temperature and density evolution are shown in Figure 5. The initial temperatures that are obtained in some of the loops after they are heated are extremely high ($\sim 10^{10}$ K) and are therefore unphysical. These high temperatures are a result of the fact that the Cargill model does not apply to the thin layer on the surface of the loop system where strong evaporative flows are occurring. We plan to address the dynamic behavior of this layer in a future study using a full hydrodynamic loop model. In any case, the layer of high temperatures is extremely thin because the conduction cooling time is extremely rapid at such high temperatures. Thus, the bulk of the arcade is well approximated using the Cargill model, and for the strong (120 G) background field case most of the plasma is around 25 MK, which is a reasonable value for a large flare.

The density is mostly concentrated in the loops at the bottom of the arcade, where the loop temperatures are 20–30 MK, and not in the upper, more cusp-shaped loops where the temperatures are higher. This distribution of density in the arcade of loops is due to the amount of time it takes to fully evaporate the chromospheric plasma into each loop. In the Cargill model evaporation takes place during the entire conductive cooling phase; therefore, a loop will reach its maximum density some time after it is reconnected.

Once the temperatures and densities in each loop have been calculated, they are used to determine the intensities in the

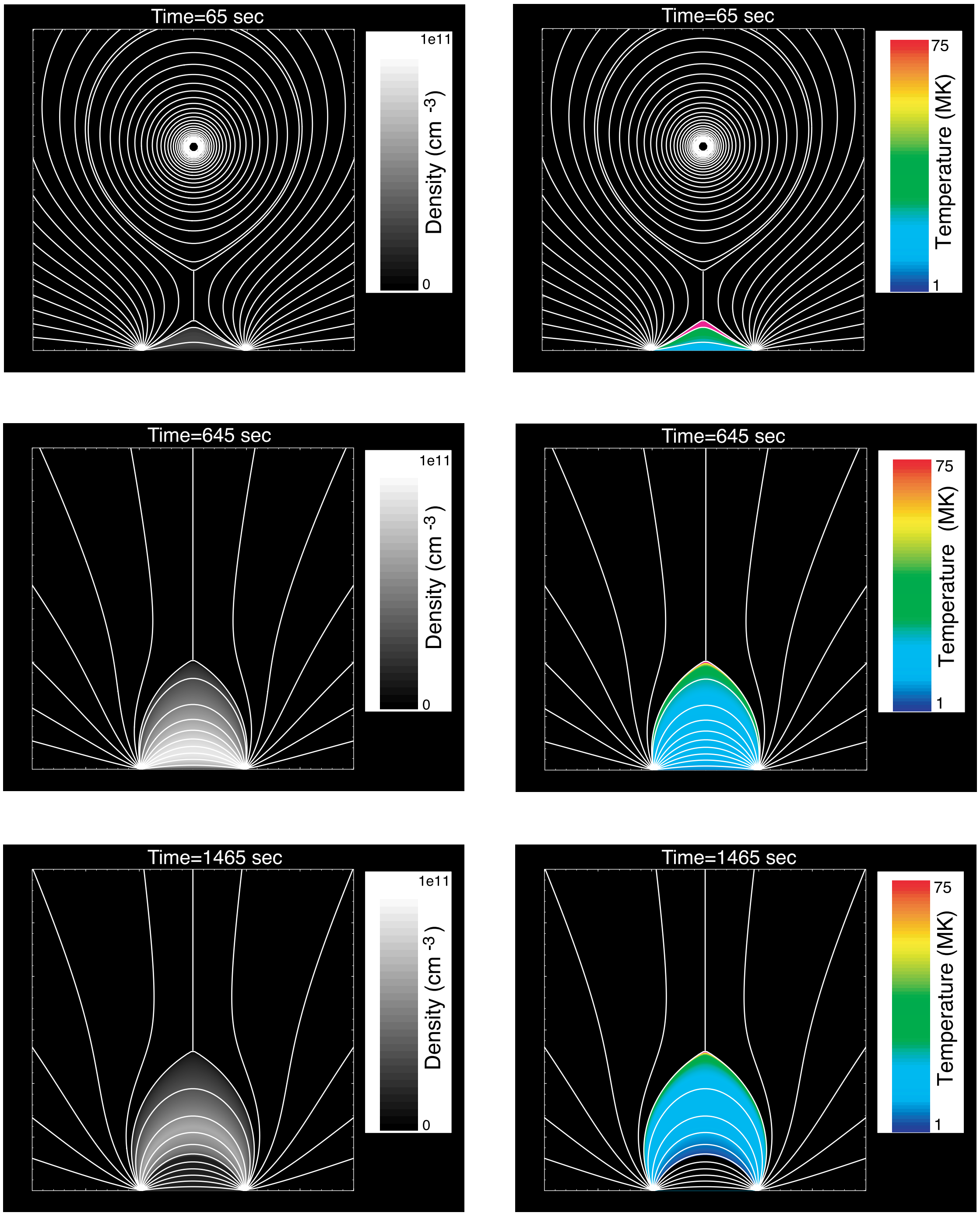

FIG. 5.—Density (*left panels*) and temperature (*right panels*) evolution for the case with a background field of 120 G. The times at the top of each frame are the time passed since the formation of the X-point.

Transition Region and Coronal Explorer (*TRACE*), the Soft X-Ray Telescope (SXT) on *Yohkoh*, and the *Geostationary Operational Environmental Satellite* (*GOES*) using the standard SolarSoft routines `trace_euv_resp`, `sxt_flux`, and `goes_fluxes`.[1] These routines take a plasma temperature and emission measure and fold them through the instrument response function to obtain the intensity that would be observed in that instrument. The SXT and *GOES* routines both require a volume emission measure, given by $n^2\,dV$, where n is the electron number density. For SXT a volume, dV, consisting of the thickness of the loop multiplied by the area of an SXT pixel, is used. Since *GOES* monitors the whole Sun, a dV consisting of the thickness of the loop times the approximate area of the flare, $2\lambda_0 L$, is used. To get *TRACE* intensities, a line-of-sight emission measure, given by $n^2\,dl$, is required, so the thickness of the loops is used as dl. The thickness of the loops was determined by calculating the distance between consecutive reconnected field lines in the lower set of loops.

We calculate the intensity near the peak of the event using the SXT AlMg filter for arcades with strong (120 G) and weak (12 G) background field strengths and show the resulting images in Figure 6. We have assumed exposure times such that the peak

[1] See Freeland & Handy (1998) and http://www.lmsal.com/solarsoft for more information on the SolarSoft software package.

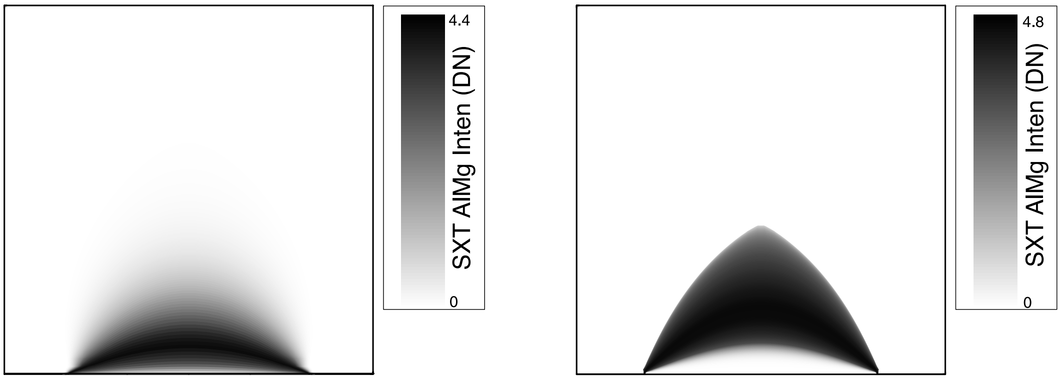

FIG. 6.—Snapshots of the intensity of the arcade in the SXT AlMg filter for the 120 (*left*) and 12 G (*right*) background field cases. Snapshots were taken around the time of maximum intensity in both cases. Simulated exposure times were taken to be 0.02 ms for the 120 G case and 1 s for the 12 G case so that the peak normalized counts are similar.

normalized counts are approximately the same in each image. In the 120 G background field case the loops that contribute most to the intensity are in the lower part of the arcade, where the bulk of the density is found. These loops have been cooling and evaporating plasma for some time, and the density in these loops is several orders of magnitude higher than the loops that have just reconnected near the cusp region. Because of the large difference in density between the newly reconnected loops in the cusp region and the loops lower down, SXT may not be able to image the plasma in the cusp region without saturating the detector in the lower part of the arcade. This example, shown in the top panel of Figure 6, illustrates a situation in which reconnection is occurring at the top of the arcade, but cusp-shaped loops would not necessarily be observed.

The weak-field case shown in Figure 6, on the other hand, does exhibit a cusplike character. In this case, because the energy release rate is slower, the chromospheric evaporation is more gentle, and less material is evaporated into the loops. Thus, the peak intensity of a loop is of the same order of magnitude as the intensity in loops that have just reconnected, and SXT is easily able to image the plasma in both the cusp region and the lower part of the arcade. This outcome is consistent with observations of cusp-shaped loops in SXT, since these loops are often observed in weak flares (e.g., Hudson et al. 1996; Forbes & Acton 1996) and, as is shown below, this case amounts to an A flare in the *GOES* flare classification scheme.

Using the intensities calculated in the arcade of loops, we construct some sample light curves for *TRACE*, SXT, and *GOES*, shown in Figure 7. For the *TRACE* light curves we use the 195 Å filter, and for the SXT light curves we use the Be119 filter, both of which are commonly used to observe flares. For the *GOES* light curve we choose the 1–8 Å channel, which is the channel used to classify flares as A, B, C, M, or X. The plasma in the corona is optically thin, so the intensities of each part of a loop along a given line of sight contribute to the total intensity in a pixel for the imaging instruments. We take the line of sight for the SXT and *TRACE* light curves to be directly above the apex of the loops, as if the loops were located at disk center. *GOES* is a full-Sun instrument, as mentioned before, so no line of sight needs to be specified.

The *TRACE* and SXT light curves for the case with the 120 G background magnetic field (plotted by a solid line in the top two panels of Fig. 7) have features similar to those of observed light curves, including rapid rise phases and long decay-phase tails (see, e.g., Reeves & Warren 2002; Aschwanden & Alexander 2001). The presence of a spike in the *TRACE* 195 Å curve but the absence of a corresponding spike in the SXT curve is due to the different instrument response functions of these two instruments. The *TRACE* 195 Å filter is most sensitive to plasma at about 1.5 MK. The spike in the light curve occurs because several loops in the arcade cool through a temperature of 1.5 MK at the same time, and the resulting strong intensities of these loops add to create a large increase in intensity in the light curve. Several properties of our model combine to produce this effect. First of all, the height of the loop top, p, rises very quickly initially, leading to a subsequent drop in the initial density of the first several loops that are formed. Thus, the initial conductive cooling time, $\tau_c = 4 \times 10^{10} nL/T^{5/2}$, is shorter in loops that form later, causing newly heated loops to cool through 1.5 MK before loops formed at earlier times. As the rise in p becomes more gradual, the initial conductive cooling time increases. Eventually a point is reached where many loops formed at different times pass through 1.5 MK nearly simultaneously, thus creating the spike in intensity. Because the existence of the spike strongly depends on the initial heating and evaporation processes, the spike could be an artifact of the simplifying assumptions used in the model. Particularly suspect is the assumption that newly reconnected loops are heated instantaneously. Future work using hydrodynamic codes could help resolve this issue.

The light curves for the case with the 12 G background field (plotted by a dashed line in the top two panels of Fig. 7) have a much lower peak intensity in both *TRACE* and SXT. Note that the light curves for the case with the 12 G background field have been multiplied by large factors in Figure 7 to make them visible on the plot. The *TRACE* 195 Å light curve for the 12 G background field case has a peak intensity of 20 DN s^{-1}, which is on the same order of magnitude as the peak intensities in active region loops (Winebarger et al. 2003; Aschwanden et al. 2000) but fainter than typical flare intensities. The SXT Be119 filter is not often used to observe such faint loops, but Tsuneta et al. (1991) estimate that an active region would have an intensity of about 4 DN s^{-1} in this filter, so the SXT light curve for the weak background magnetic field case is also consistent with an active region loop intensity. Also, the light curves associated with the 12 G background magnetic field in both instruments increase in intensity gradually with time; they do not exhibit the rapid increase in intensity normally associated with flare light curves.

The bottom panel in Figure 7 shows the simulated light curves for the 1–8 Å channel in *GOES*, with two different levels of background flux added. The simulated flares are positioned so

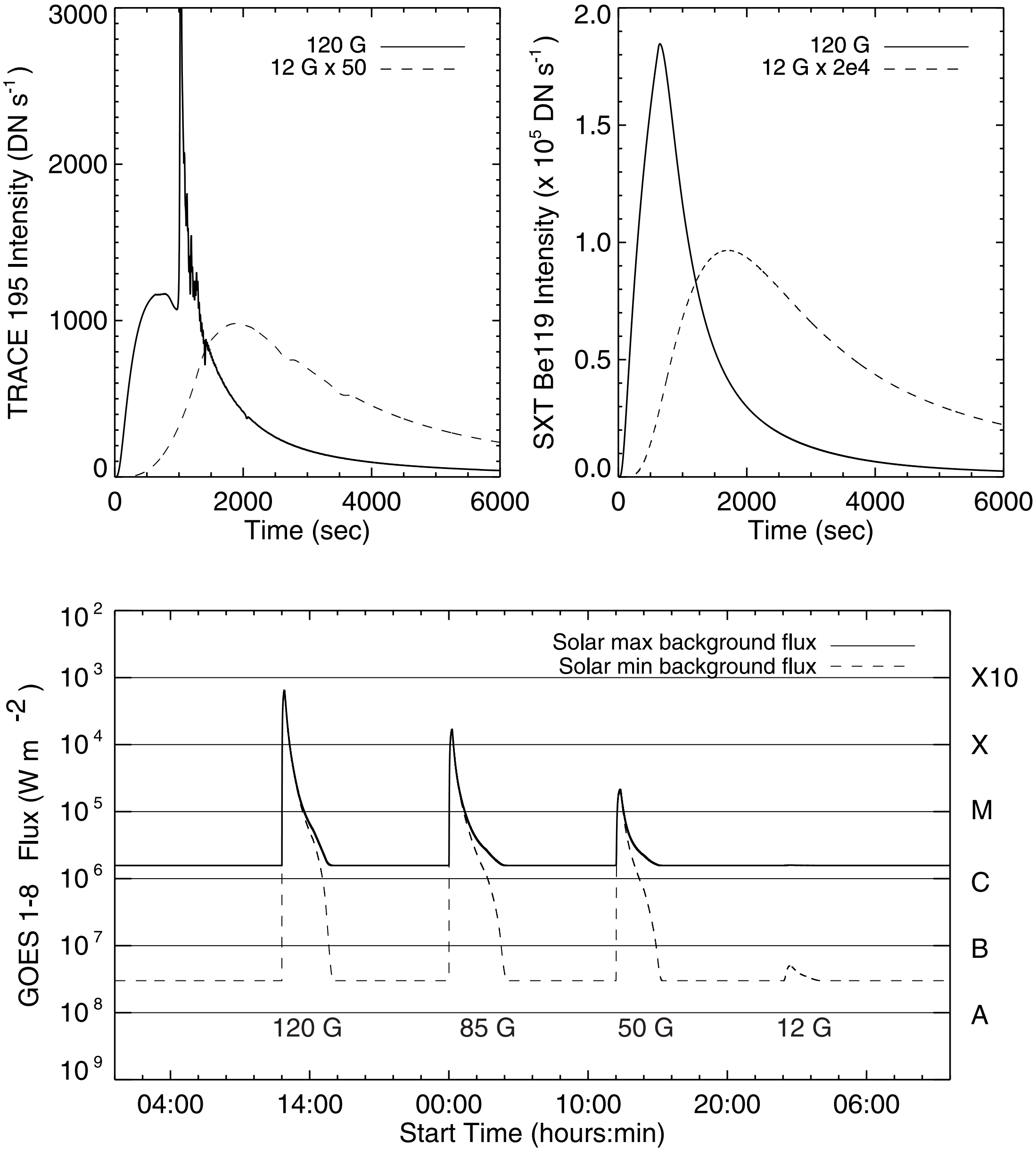

Fig. 7.—Simulated light curves for the *TRACE* 195 Å filter (*top left*), *Yohkoh* SXT Be119 filter (*top right*), and *GOES* 1–8 Å channel (*bottom*). In the top panels, the solid line is the light curve for the case with the 120 G background field, and the dashed line is the case with the 12 G background field. Note that intensity in the 12 G case has been multiplied by 50 in the *TRACE* light curve and 2×10^4 in the SXT light curve. In the bottom panel, simulated light curves corresponding to background fields of 120, 85, 50, and 12 G begin every 12 hr. Light curves including background X-ray flux levels consistent with solar maximum (*solid line*) and solar minimum (*dashed line*) are shown.

that they start every 12 hr. The light curve for the 120 G background field case is presented first, then the 85, 50, and 12 G. The light curves with the solid line have an added background flux of 1.5×10^{-6} W m^{-2}, and the dotted line has an added background flux of 3×10^{-8} W m^{-2}. The larger background value is the maximum average X-ray flux rate seen in the 1–8 Å channel by *GOES* during solar cycle 22, and the smaller background value is the minimum average X-ray flux rate during that same cycle (Wilson 1993). Also indicated are the levels of flux needed for a flare to be designated an A, B, C, M, or X class flare.

In the case of the light curves with the high background X-ray flux, the light curve from the 12 G case is hardly discernible above the background and would probably not be considered a flare. The 12 G case is more visible in the curves with the low background level and in that case has a peak *GOES* flux of 5×10^{-8} W m^{-2}, making it an A5 flare in the *GOES* flare class designation scheme.

As shown in Figure 2, the case with the 12 G background field strength has a speed of about 300 km s^{-1}. Studies correlating flare occurrence with CME speed have found that slow CMEs are less likely to be associated with a flare than fast CMEs (Gosling et al. 1976; Moon et al. 2002). When these studies use *GOES* data, typically a minimum *GOES* class of C1 is required for an event to be considered a flare (e.g., Sheeley et al. 1983; Moon et al. 2002). Thus, the X-ray emission for the CME with the background field of 12 G is more than an order of magnitude fainter than the faintest flares used in correlation studies and for active parts of the solar cycle would be overwhelmed by the background flux.

The light curves presented in Figure 7 suggest that this model does not necessarily predict a flare associated with every CME. In particular, the 12 G background field case, corresponding to a CME with a speed of $\sim$300 km s^{-1}, does not release enough

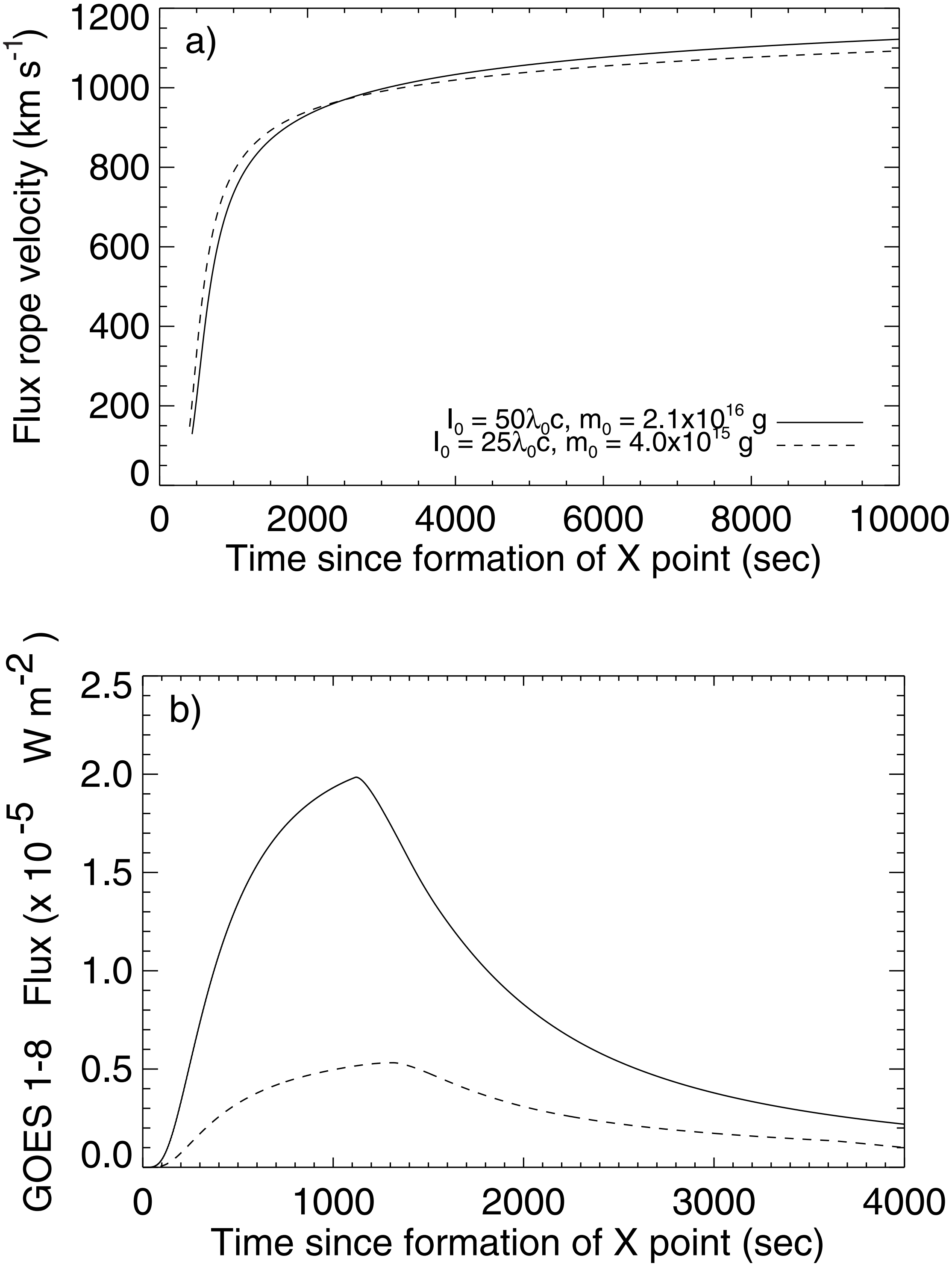

Fig. 8.—(*a*) Velocity profile of the flux rope for a case with a 50 G background field and a flux rope mass of 2.1×10^{16} g (*solid line*) and a case with a 25 G background field and a flux rope mass of 4×10^{15} g (*dashed line*). (*b*) Simulated *GOES* light curves for the same two cases.

thermal energy to heat and evaporate sufficient plasma into the lower set of loops to produce a substantial EUV brightening. *TRACE* and SXT would see a slow brightening to a mild intensity about the same as an active region loop, and in *GOES* the emission would be insignificant compared to the usual X-ray background flux levels in all but the quietest parts of the solar cycle.

Since fast CMEs are not necessarily always associated with large flares (see, e.g., Vršnak et al. 2005), we have also calculated the *GOES* 1–8 Å light curve for a case that has a similar flux rope velocity to the 50 G background field case but produces a much smaller flare. The flux rope velocities and light curves are shown in Figure 8. The solid line is the case with a 50 G background field and the same parameters that are given at the beginning of this section. The dotted line is a case with a 25 G background field and a flux rope mass of 4×10^{15} g. The other parameters are the same. The velocity profiles of the flux ropes are very similar in these two cases, but the *GOES* light curves are quite different. The case with the lower background magnetic field strength and

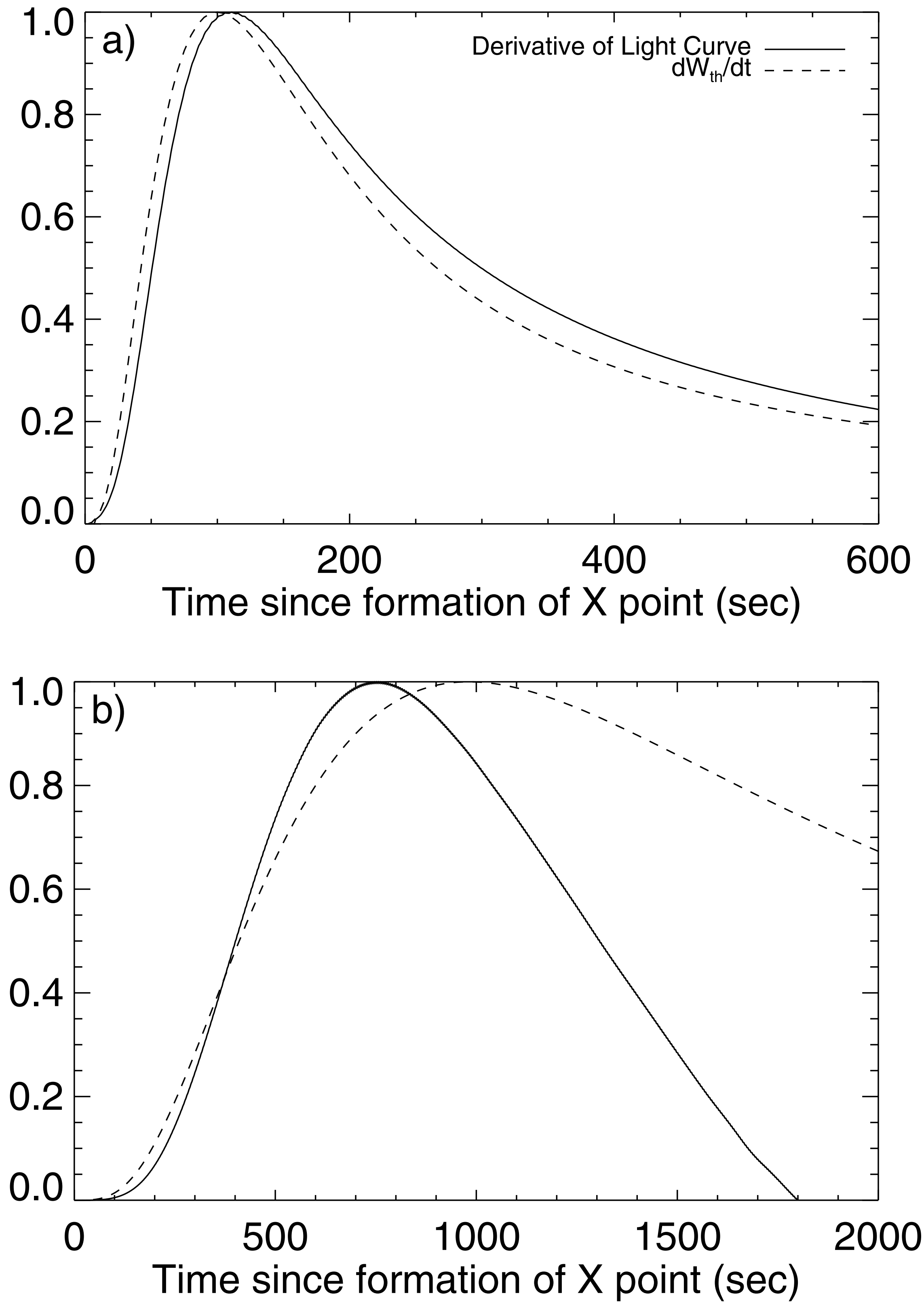

FIG. 9.—Derivative of the *GOES* 1–8 Å light curve (*solid line*) and thermal energy release rate (*dashed line*). (*a*) Case with a 120 G background field. (*b*) Case with a 12 G background field.

mass has a peak *GOES* flux equivalent to a C5 flare, compared to an M2 flare for the larger background field strength and mass.

Figure 8 shows that CME speed is not indicative of the amount of associated X-ray emission from the lower set of loops. The amount of thermal energy released in the current sheet in this model is directly related to the strength of the background magnetic field, while the kinetic energy of the flux rope depends on the mass and the background magnetic field strength. Therefore, a relatively low mass CME from a weak-field region can have a similar velocity profile to a massive CME from a stronger background magnetic field region, and the difference in the physical properties of the situation will manifest in the X-ray emission observed in the post-flare loops.

3.3. *The Neupert Effect*

Our model allows us to examine the relationship between the thermal energy release rate and the soft X-ray flux, and it has implications for what is often referred to as the Neupert effect. This effect is an empirical relation that states that a flare's microwave emissions are proportional to the derivative of its soft X-ray light curve (Neupert 1968). It has been extended to relate to hard X-ray light curves and microwaves since emissions in both wavelength regimes are thought to be produced by the same non-thermal population of accelerated particles. One implication of the Neupert effect is that $dW_{\rm th}/dt \propto dI_{\rm SXR}/dt$ (Takasaki et al. 2004). This relation follows from the fact that in the Neupert effect the energy release rate and the time rate of change of the soft X-ray intensity are both proportional to the hard X-ray intensity. However, a recent study by Warren & Antiochos (2004) has found that using the Cargill et al. (1995) model for the cooling of a flare loop gives

$$I_{\rm SXR} \propto W_{\rm th}^{1.75}/V^{0.75}L^{0.25} \qquad (35)$$

for the *GOES* 1–8 Å instrument, where L is the length of the flare loop and V is the volume of the flare. This result appears to contradict the Neupert effect, which predicts that $I_{\rm SXR} \propto W_{\rm th}$ (Lee et al. 1995). This contradiction can be reconciled, however, by the fact that equation (35) only applies to a single loop, whereas the Neupert effect applies to the entire arcade.

Figure 9 shows normalized curves for $dW_{\rm th}/dt$ and the derivative of the *GOES* 1–8 Å light curve for the 120 G background field case and the 12 G background field case. For the 120 G background field case there is very good agreement between the derivative of the light curve and $dW_{\rm th}/dt$. This result may seem surprising at first, given that we are using the Cargill cooling, which implicitly incorporates equation (35). Our model flare is made up of an arcade of many different loops that have different start times with different energy inputs. Furthermore, the volume of the flare increases dramatically with time (see Fig. 5), which affects the relationship between $I_{\rm SXR}$ and $W_{\rm th}$ given by equation (35). The increase in flare volume causes the derivative of equation (35) to peak earlier and decline faster than if the volume were considered to be a constant, which is consistent with our results. Therefore, even though the intensity in each individual loop in our arcade obeys the scaling law derived by Warren & Antiochos (2004), the derivative of the light curve of the aggregate arcade gives a result that is more consistent with the Neupert effect, at least in this particular case.

Not all observed flares follow the behavior predicted by the Neupert effect, however. Large flares tend to behave in a way that agrees with the Neupert effect more often than weak flares (Veronig et al. 2002), and high-temperature plasma ($\geq$16.5 MK) exhibits the Neupert effect better than low-temperature plasma (McTiernan et al. 1999). The weak background field case produces a lower set of loops that are mostly filled with plasma below 20 MK, and it produces a very weak flare, making it an interesting case to look at in light of the above findings regarding the Neupert effect. Examining the curves for this case, shown in Figure 9, we note that there is a discrepancy between the timing of the peak of the energy release rate and the peak of the derivative of the light curve. One possible explanation for the deviation of events from the Neupert effect is that the energies involved are not accurately represented by the soft and hard X-ray light curves (Veronig et al. 2002; Lee et al. 1995). The results for the weak-field case in Figure 9 lend evidence to support this explanation.

4. CONCLUSIONS

In this paper we have extended the model of Lin & Forbes (2000) by calculating the Poynting flux into the current sheet and assuming that the resulting energy is thermalized and heats the plasma in the flare loops. We find that the fraction of the released energy that is converted to thermal energy depends on the inflow Alfvén Mach number; greater than 50% of the released energy becomes thermal energy when $M_{\rm A} < 0.006$. In the limit that $M_{\rm A} \rightarrow \infty$, the fraction of released energy that becomes thermal energy goes to zero. The behavior of the system in the opposite limit, when $M_{\rm A} \rightarrow 0$, is not clear because of peculiarities of our model related to its two-dimensional nature. A three-dimensional model based on similar principles would not have the same problems and may be able to determine a value for $M_{\rm A}$ such that the fraction of released energy that is converted into thermal energy is maximized.

The calculated thermal energy in the current sheet can be used to calculate initial temperatures and densities in the flare loops, which can then in turn be used to calculate the evolution of these quantities using the Cargill cooling model. This method is a very simple way to get temperatures and densities in the loops, although there are some inherent problems with it. Our calculation of the initial temperatures for the loops gives some unrealistically high temperatures, and the Cargill cooling model results in very rapid initial evaporation of chromospheric material. Another drawback of this method is that is assumes that the conductive and radiative cooling can be separated, causing the cooling to be solely conductive at first and solely radiative at later times. We plan to address these problems in the future by using a full hydrodynamic code to calculate the characteristics of the flare loops.

Even with some of the limitations of the Cargill method of calculating temperatures and densities in the loops, we find that the model well accounts for the observed shape of flare light curves, including the rapid increase in intensity at the start of the flare and the long duration of the late phase emission. This model represents an enhancement to the previous multiloop model that used the Cargill cooling scheme to calculate light curves (Reeves & Warren 2002) in two respects. First of all, the thermal energy input for the loops in the current work is based on theoretical calculations that result in different initial temperatures and densities in each loop. The previous model assumed that the initial temperatures and densities were the same in every loop, thereby overestimating the total energy input into the flare. Secondly, the previous model was unable to reproduce the decay-phase tail on the *TRACE* and SXT light curves, possibly because of the assumptions made about the loop thicknesses.

We find that the intensity of the resulting EUV emission is dependent on the strength of the background magnetic field. For weak background field strengths, the emissions are quite faint and in some cases would probably not be classified as flares. This finding supports the idea that there is a continuum of eruptive solar phenomena encompassing fast, flare-associated CMEs and slow, non–flare-associated CMEs (e.g., Vršnak et al. 2005). On the other hand, we find that CMEs with very similar trajectories can have quite different flare responses depending on the background magnetic field strength, the inflow Alfvén Mach number, and the flux rope mass.

Furthermore, we find that the thermal energy release rate agrees very well with the derivative of the soft X-ray light curve for a case with a large background magnetic field strength, which is the required result if the Neupert effect is real. This result is somewhat unexpected, however, given that Warren & Antiochos (2004) found that loops cooled using the Cargill formalism result in a scaling law between soft X-ray flux and thermal energy that is inconsistent with the Neupert effect. The discrepancy is probably due to the fact that our light curves are constructed from the intensities of hundreds of loops with different input energies, start times, and lengths, whereas Warren & Antiochos (2004) only considered one loop. In the weak background field case the derivative of the light curve does not match the energy release rate, which supports the idea that the Neupert effect does not hold in some cases because the soft X-ray flux is not always proportional to the thermal energy.

The authors would like to thank the anonymous referee for helpful comments on the manuscript. This work was supported by NSF grant ATM 03-27512 and NASA LWS TR&T grant NNH05AA13I to the University of New Hampshire, as well as DoD MURI grants to the University of California at Berkeley and to the University of Michigan.

REFERENCES

Antiochos, S. K., & Sturrock, P. A. 1978, ApJ, 220, 1137
Aschwanden, M. J., & Alexander, D. 2001, Sol. Phys., 204, 91
Aschwanden, M. J., Nightengale, R. W., & Alexander, D. 2000, ApJ, 541, 1059
Cargill, P. J., Mariska, J. T., & Antiochos, S. K. 1995, ApJ, 439, 1034
Dere, K. P. 1996, ApJ, 472, 864
Forbes, T. G. 2003, Adv. Space Res., 32, 1043
Forbes, T. G., & Acton, L. W. 1996, ApJ, 459, 330
Forbes, T. G., & Isenberg, P. A. 1991, ApJ, 373, 294
Forbes, T. G., & Priest, E. R. 1995, ApJ, 446, 377
Forbes, T. G., Priest, E. R., & Isenberg, P. A. 1994, Sol. Phys., 150, 245
Freeland, S. L., & Handy, B. N. 1998, Sol. Phys., 182, 497
Gosling, J. T., Hildner, E., MacQueen, R. M., Munro, R. H., Poland, A. I., & Ross, C. L. 1976, Sol. Phys., 48, 389
Hori, K., Yokoyama, T., Kosugi, T., & Shibata, K. 1997, ApJ, 489, 426
———. 1998, ApJ, 500, 492
Hudson, H. S., Acton, L. W., & Freeland, S. L. 1996, ApJ, 470, 629
Isenberg, P. A., Forbes, T. G., & Demoulin, P. 1993, ApJ, 417, 368
Lee, T. T., Petrosian, V., & McTiernan, J. M. 1995, ApJ, 448, 915
Lin, J. 2001, Ph.D. thesis, Univ. New Hampshire
———. 2002, Chinese J. Astron. Astrophys., 2, 539
———. 2004, Sol. Phys., 219, 169
Lin, J., & Forbes, T. G. 2000, J. Geophys. Res., 105, 2375
Lin, J., Forbes, T. G., Isenberg, P. A., & Demoulin, P. 1998, ApJ, 504, 1006
McTiernan, J. M., Fisher, G. H., & Li, P. 1999, ApJ, 514, 472
Moon, Y.-J., Choe, G. S., Wang, H., Park, Y. D., Gopalswamy, N., Yang, G., & Yashiro, S. 2002, ApJ, 581, 694
Neupert, W. M. 1968, ApJ, 153, L59
Priest, E. R., & Forbes, T. G. 1992, J. Geophys. Res., 97, 16757
Reeves, K. K., & Forbes, T. G. 2005, in IAU Symp. 226, Coronal and Stellar Mass Ejections, ed. K. P. Dere, J. Wang, & Y. Yan (Cambridge: Cambridge Univ. Press), 250
Reeves, K. K., & Warren, H. P. 2002, ApJ, 578, 590
Sheeley, N. R., Howard, R. A., Koomen, M. J., & Michels, D. J. 1983, ApJ, 272, 349
Sittler, E. C., & Guhathakurta, M. 1999, ApJ, 523, 812
Sturrock, P. A., Weber, M., Wheatland, M. S., & Wolfson, R. 2001, ApJ, 548, 492
Takasaki, H., Asai, A., Kiyohara, J., Shimojo, M., Terasawa, T., Takei, Y., & Shibata, K. 2004, ApJ, 613, 592
Tsuneta, S., et al. 1991, Sol. Phys., 136, 37
Veronig, A., Vršnak, B., Dennis, B. R., Temmer, M., Hanslmeier, A., & Magdalenić, J. 2002, A&A, 392, 699
Vršnak, B., Sudar, D., & Ruždjak, D. 2005, A&A, 435, 1149
Warren, H. P., & Antiochos, S. K. 2004, ApJ, 611, L49
Wilson, R. M. 1993, J. Geophys. Res., 98, 11477
Winebarger, A. R., Warren, H. P., & Seaton, D. B. 2003, ApJ, 593, 1164
Yokoyama, T., Akita, K., Morimoto, T., Inoue, K., & Newmark, J. 2001, ApJ, 546, L69
Yokoyama, T., & Shibata, K. 2001, ApJ, 549, 1160